

Effects of inhomogeneities on pinning force scaling in Nb₃Sn wires

T Baumgartner¹ , S Pfeiffer², J Bernardi² , A Ballarino³ and M Eisterer¹ 

¹ Atominstytut, TU Wien, Stadionallee 2, 1020 Vienna, Austria

² USTEM, TU Wien, Wiedner Hauptstraße 8–10, 1040 Vienna, Austria

³ CERN, 1211 Geneva 23, Switzerland

E-mail: thomas.baumgartner@tuwien.ac.at

Received 29 March 2018, revised 23 May 2018

Accepted for publication 29 May 2018

Published 22 June 2018



Abstract

We analyzed the effects of A-15 phase inhomogeneities, in particular Sn concentration gradients, on the pinning force scaling behavior of Nb₃Sn wires. This was accomplished using a software code capable of simulating both magnetization and transport measurements on wires containing sub-elements with an arbitrary (e.g. modeled after EDX data) Sn concentration profile. We demonstrate that certain experimentally observed deviations from the ideal scaling behavior, in particular large values of the high-field scaling exponent q and the zero-temperature scaling field $B_{c2}^*(0)$ are caused by gradients in stoichiometry. In the presence of such gradients the scaling analysis results depend on the field and temperature ranges covered by the input data, and we discuss the stronger influence of inhomogeneities on magnetometry-based results. Our simulation code was benchmarked by attempting to mimic the scaling behavior of a Ti-alloyed Restack Rod Process wire observed in magnetometry experiments with a field limit of 7 T. By comparison to transport data obtained in fields of up to 15 T, we found that the simulations provide a significantly better high-field $J_c(B)$ prediction compared to an extrapolation based on conventional scaling.

Keywords: Nb₃Sn, inhomogeneity, pinning force scaling, magnetometry

(Some figures may appear in colour only in the online journal)

1. Introduction

Five decades ago, Fietz and Webb discovered that the volume pinning force $F_p = |\vec{B} \times \vec{J}_c|$ of superconducting Nb–Ti and Nb–Ta alloys obeys a scaling law, i.e. $F_p(B)$ data obtained at different temperatures can be mapped onto a single curve by a simple transformation [1]. This transformation consists of dividing the F_p values by their maximum, and the field values by a temperature dependent scaling field. If the function which normalizes the F_p values to the interval [0, 1], and the function describing the scaling field can be parametrized without mutual dependences, the scaling law is said to be separable [2]. If such a separable scaling law is applicable,

data obtained within a particular temperature and field range can easily be used to calculate the volume pinning force at temperature and field values outside of this range. Clearly, this is a highly attractive quality in terms of characterization and engineering, which explains the popularity of separable scaling laws, in particular in view of the application of conductors based on Nb₃Sn—a material whose scaling behavior has been studied extensively.

In the following we will use the formalism of the so-called unified scaling law (USL), which is a unification of the temperature scaling law of Fietz and Webb with the strain scaling law, described in a series of review articles by Ekin [2–4]. The USL uses the parameterization

$$F_p(\varepsilon_0, t, b) = C g(\varepsilon_0) h(t) f(b), \quad (1)$$

where C is a constant, $g(\varepsilon_0)$ describes the strain dependence, $h(t)$ the temperature dependence, and $f(b)$ the field



Original content from this work may be used under the terms of the Creative Commons Attribution 3.0 licence. Any further distribution of this work must maintain attribution to the author(s) and the title of the work, journal citation and DOI.

dependence of the volume pinning force. The latter, which is often referred to as the pinning force function, is cast in the form

$$f(b) = b^p (1 - b)^q, \quad (2)$$

with the field scaling exponents p and q determining its shape. These two parameters must not possess any field, temperature, or strain dependence, since shape invariance of the function $f(b)$ is a prerequisite for scaling. The temperature dependence in its most general form is given by

$$h(t) = (1 - t^2)^\mu (1 - t^\nu)^{\eta-\mu}, \quad (3)$$

where the term $1 - t^2$ stems from the two-fluid model temperature dependence of the thermodynamic critical field, and $1 - t^\nu$ approximates the temperature dependence of the upper critical field. The exponent μ is fixed to a value of 0, 1, or 2, depending on the particular scaling model. The other two temperature scaling exponents are either used as free parameters, or also fixed to model dependent values [2].

The reduced field and temperature used in the above equations are defined as

$$b = \frac{B}{B_{c2}^*(t, \varepsilon_0)} \quad \text{and} \quad t = \frac{T}{T_c^*(\varepsilon_0)}, \quad (4)$$

where B_{c2}^* and T_c^* are the scaling field and the effective critical temperature, which are in general not equal to the upper critical field B_{c2} and the critical temperature T_c , respectively. Since the strain dependence is outside the focus of this paper, the function $g(\varepsilon_0)$ will not be discussed here, and the dependences on the intrinsic strain ε_0 in equation (4) will be disregarded in the following. We will therefore replace equation (1) by

$$F_p(t, b) = F_p^0 C_f h(t) f(b), \quad (5)$$

where F_p^0 is the maximum volume pinning force (peak of the $F_p(B)$ curve at zero-temperature), and C_f normalizes $f(b)$ to a peak value of 1 ($h(t)$ always satisfies $\max(h(t)) = h(0) = 1$). Grain boundary pinning is generally accepted as the dominant contribution to the volume pinning force in Nb_3Sn . Theoretically, as shown by Dew-Hughes, this pinning mechanism gives rise to the field scaling exponents $p = 0.5$ and $q = 2$ [5]. In Dew-Hughes' derivation, p stems from the pinned length of flux lines per unit volume (which is assumed to be inversely proportional to their spacing, and consequently proportional to \sqrt{B}), and mainly affects the low-field behavior of $f(b)$. The exponent q stems from the field dependence of the superconducting order parameter, and is responsible for the high-field behavior of the pinning force function.

In reality, however, significant deviations from the expected scaling behavior can occur. Scaling exponents different from the theoretical values are commonly found, and unrealistically high scaling field values at low temperatures are sometimes reported [2–4]. In this article we show that these deviations can be attributed to A-15 inhomogeneities, in particular Sn concentration gradients within the sub-elements of Nb_3Sn wires. Our arguments are based on simulations which break up the inhomogeneous Nb_3Sn into finite, homogeneous elements, assuming that each of these elements

exhibits ideal scaling properties. By emulating the processes from which (the averaged macroscopic) J_c is obtained from either transport measurements or magnetometry, we were able to work out the different impacts of inhomogeneities on these two types of measurements. While inhomogeneities have been known for a while to affect scaling, and some work on simulating their impact has been carried out (most notably [6] by Cooley *et al*), the present work is to our knowledge the most detailed analysis of the problem, and does, unlike previous contributions, highlight the important differences between transport measurements and magnetometry.

In section 2 we first provide experimental details on how we obtained pinning force data as well as information on A-15 inhomogeneity from a real wire which serves as a reference for our simulations. After that, the simulation code, and the procedure for analyzing the pinning force scaling behavior are discussed. Our results are presented in section 3, starting with the deviations from the expected scaling behavior found in the real wire, and a simulation-based analysis of the effects of inhomogeneities on the scaling parameters. The ability of the simulation software to mimic the behavior of the real wire is demonstrated, sources of deviations between magnetometry- and transport-based scaling analyses are identified, and the influence of the analyzed temperature range is discussed. In section 4 we discuss the practical relevance of our results, and put our findings in context with research done by others. The main conclusions of our work are presented in section 5.

2. Experiments, simulations, and analysis

The wire investigated in the measurements described below is a Ti-alloyed Restack Rod Process (RRP) strand containing 108 sub-elements. It received a heat treatment of 210 °C for 48 h, followed by 400 °C for 48 h and a final stage of 665 °C for 50 h, the ramp rates being 50 °C h⁻¹ (up), and 100 °C h⁻¹ (down), respectively. We also have pinning force data obtained from other wire types (Ta-alloyed RRP as well as powder-in-tube (PIT)), some of which show more pronounced deviations from the theoretical grain boundary pinning scaling behavior. The Ti-alloyed RRP wire is, however, the only one from which we have transport critical current data, which is important in the context of this work for comparison with the magnetometry-based scaling analysis.

2.1. Magnetometry

The $J_c(T, B)$ data on which our pinning force scaling analyses of the above-mentioned wire are based were obtained from magnetometry. There are several good reasons for choosing magnetometry instead of transport measurements for such a task, including the simplicity of the experimental procedure, and the possibility to obtain data in temperature and field ranges where the critical current would be too high for the available transport set-up. An additional, and quite crucial, advantage arises from the small sample size when the measurements are part of an irradiation study, the samples thus

being radioactive. It is also convenient that a first-order self-field correction is inherent to magnetometry. The irreversible magnetic moment m_{irr} is obtained by subtracting the moments measured in increasing and in decreasing field, and the polarity of the self-field is different in the two cases. Therefore, only errors stemming from the local nonlinearity of $m_{\text{irr}}(B)$ remain, which are small enough to neglect, with the exception of applied field values close to zero.

Our magnetization measurements were carried out using a Quantum Design MPMS XL SQUID magnetometer equipped with an RSO (Reciprocating Sample Option). Three samples with a length of 4 mm were cut from a straight piece of wire, aligned perpendicular to the applied magnetic field, and magnetization loops were recorded at 12 different temperatures (4.2, 5, 6, ..., 15 K) using field steps of 0.2 T. The critical current density J_c was obtained from m_{irr} using the evaluation procedure described in [7]. The model underlying this procedure assumes that the proportionality factor relating J_c to m_{irr} depends only on the (effective) inner and outer radii of the A-15 region of the sub-elements, the sample length, and the number of sub-elements. It assumes a spatially constant J_c within the A-15 region, and cannot account for any inhomogeneities.

The main disadvantage of the way we obtained $J_c(T, B)$ data from magnetometry is that the maximum applied field of our SQUID magnetometer is limited to 7 T. This relatively small field range is the reason why we decided to measure at temperatures of up to 15 K in order to reach reduced field values of $b \approx 1$. Certain problems to which transport measurements are immune, such as partial magnetization profile reversal due to field inhomogeneities, and relaxation due to shaking field effects may also occur, but these effects are beyond the scope of this article. In the following we will assume flawless measurements, whose results are only influenced by the effects of A-15 inhomogeneities.

2.2. Transport measurements

Transport critical current measurements on six samples of the above-mentioned wire were carried out for comparison with the magnetometry results. The measurements were done at 4.2 K only, since the gas cooled operating mode required for measuring above liquid helium temperature could not provide sufficient temperature stability. The maximum applied field of our transport set-up is 15 T, and the maximum current we can apply is 1 kA.

The samples were wound onto Ti-6Al-4V barrels (about 50 cm of wire spread over five windings on the barrel and two additional windings on the copper contacts), and received the same heat treatment as the magnetization samples. Voltage taps were soldered to the wire with a spacing of 20 cm, and an electric field criterion of $10 \mu\text{V m}^{-1}$ was used for evaluating the critical current I_c from the I - V curves. The results were self-field corrected using an expression suggested by Bordini in [8], where the geometry of an ITER VAMAS barrel (which is similar to the ones used by us) is assumed. It approximates the self-field based on finite element computations, using the

current and the distance from the wire center to the outermost sub-element as input parameters.

The temperature dependence of the upper critical field of the wire was determined in the same system by applying a current of 100 mA, and slowly sweeping the temperature at constant applied field in the field range 0–15 T. The onsets of the transitions were determined from each of these measurements, and $B_{c2}(T)$ was evaluated using the following fit to the Werthamer–Helfand–Hohenberg (WHH; see [9–11]) temperature dependence previously published by Baumgartner *et al* [12]:

$$\begin{aligned} f_{\text{WHH}}(t) &= 1 - t - C_1(1 - t)^2 - C_2(1 - t)^4, \\ \text{with } C_1 &= 0.153, C_2 = 0.152, \\ B_{c2}(t) &= B_{c2}(0)(f_{\text{WHH}}(0))^{-1} f_{\text{WHH}}(t). \end{aligned} \quad (6)$$

2.3. Energy-dispersive x-ray (EDX) and transmission electron microscopy (TEM) examinations

For the purpose of assessing inhomogeneities in the A-15 phase of the examined wire, cross sections of the wire were prepared by cutting and polishing. The distribution of chemical elements within the sub-elements was examined by means of EDX analysis using a Quanta 250 FEG SEM. Line scans across the A-15 areas of 15 individual sub-elements were carried out in order to determine the radial variation of the concentrations of Nb, Sn, Cu, and Ti from the EDX spectra recorded in each point along the lines with a spatial resolution of approximately 100 nm. A thin lamella was lifted out of a sub-element by means of focused ion beam, and the grain size distribution within this lamella was analyzed using transmission Kikuchi diffraction.

2.4. Simulations

We developed a software code which allows investigating the effects of inhomogeneities on measurements of the critical current density. Both magnetization measurements on a short sample oriented perpendicular to the applied field, and transport measurements on a helically wound sample, can be simulated. Two simplifying assumptions were made when implementing the code. The first one is that all sub-elements within the wire are identical, meaning that only one of them needs to be simulated. The second assumption is that only radial inhomogeneities exist, i.e. the material parameters are constant within concentric shells which comprise the sub-element, and there is no variation along the length. The simulation software carries out the following operations.

- Subdivide the sub-element into concentric shells, and assign values for the Sn content and the grain size to each of them. These values are taken from a user-defined profile, which is in principle arbitrary, but can of course be based on microstructure analysis results (e.g. Sn concentration gradient obtained from EDX).
- Calculate the critical temperature T_c and the upper critical field B_{c2} of each shell based on its Sn content β (described below).

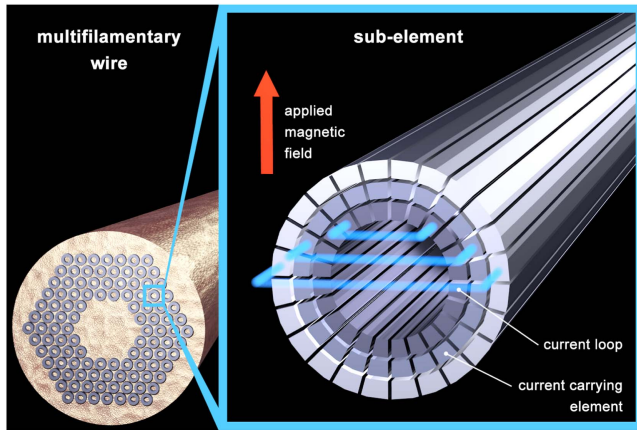


Figure 1. A single sub-element is simulated representatively for the whole wire. It is subdivided radially into shells, and angularly into current carrying elements. The current loops shown here refer to magnetometry conditions.

- Subdivide each shell angularly into current carrying elements. This step is necessary because in magnetometry simulations the self-field breaks the radial symmetry of the problem.
- For each temperature and applied field value of interest, compute J_c of each current carrying element based on its T_c , B_{c2} , and grain size, assuming grain boundary pinning. The lowest applied field is always chosen such that full penetration of the sub-element is guaranteed. Using the obtained J_c values, calculate the self-field, add it to the applied field, and iterate the J_c values.
- Compute the output data, i.e. the J_c values which would be measured in the respective experiment. In transport simulations the output J_c value is obtained by adding up the currents in all elements, and dividing by the sub-element cross section. In magnetometry simulations, the magnetic moment generated by these currents in increasing and in decreasing applied field is computed, and J_c is obtained from the resulting irreversible moment in the same way as in real experiments (see section 2.1).

Simulations using a shell-based model have been carried out before by Cooley *et al* [6]. However, their simulations were restricted to coaxially applied fields, and self-field effects were not considered. The subdivision of a sub-element used in our simulations is illustrated in figure 1, where for the sake of clarity only a small number of current carrying elements is shown. Typically, the simulation code uses 50 shells, each of them subdivided into 48 current carrying elements. In magnetometry simulations, current loops (indicated by blue lines in the image) are formed by two elements within the same shell, which are opposite to each other relative to the vertical symmetry axis, which is parallel to the applied field. For symmetry reasons, only one quarter (a quadrant of the sub-element cross section) of these 2400 elements needs to be considered in the computations.

For calculating $T_c(\beta)$ and $B_{c2}(\beta)$ the software uses the model described by Li and Gao in [13]. In the cited work, the authors used Ginzburg–Landau–Abrikosov–Gor’kov theory

to obtain the zero-temperature upper critical field based on polynomial fits to experimental data on T_c , specific heat, and normal state resistivity as a function of Sn content. After calculating T_c and $B_{c2}(0)$ based on [13], $B_{c2}(T)$ is computed using equation (6). It is well known that the presence of additives such as Ta or Ti affects the functional dependences of $T_c(\beta)$ and $B_{c2}(\beta)$ [14, 15]. This influence is, however, beyond the scope of the model, and is therefore currently neglected in our simulations.

Simulations using other models for computing the intrinsic properties were carried out for comparison. The model developed by Mentink *et al* is of particular interest, because it is based on *ab initio* calculations and microscopic theory, and does not require fits to experimental data [16]. However, it is only applicable to Nb_3Sn in the cubic phase, i.e. for material which is far enough away from stoichiometry (below approx. 23.9 at% Sn content according to this model). In [17] Godeke provides empirical fit formulas for T_c and B_{c2} as a function of Sn content. Using these equations to model the intrinsic properties yields results very similar to those obtained with the Li–Gao model.

In the same publication Godeke gives an expression for the maximum pinning force as a function of grain diameter d , which is a fit to experimental data (equation (15) for J_c data normalized to the A-15 cross section). This expression suffers from the problem that it becomes negative for grain sizes above ~ 800 nm. Since layers with grain sizes above $1 \mu m$ can be found in PIT wires, we decided to use an expression which covers a larger grain size range. We fit the following expression to the same data Godeke based his fit on (originally from [18]), plus one data point we obtained by magnetometry on a Nb_3Sn bulk sample with a grain size of $20 \mu m$:

$$F_p^0 = \frac{C_1}{d} e^{-C_2 d} + C_3. \quad (7)$$

The resulting fit parameters are $C_1 = 8.95 \times 10^3 \text{ N m}^{-2}$, $C_2 = 986 \text{ m}^{-1}$, and $C_3 = 4.44 \times 10^9 \text{ N m}^{-3}$, and the function agrees within 20% with Godeke’s equation over the grain size range 95–470 nm.

B_{c2} , T_c , and F_p^0 are used to calculate J_c of each current carrying element using equation (5), after obtaining the reduced quantities $b = B/B_{c2}$ and $t = T/T_c$. For the pinning force function term $f(b)$ the scaling exponents $p = 0.5$ and $q = 2$ are used in accordance with the assumption of grain boundary pinning [5]. The temperature dependence $h(t)$ is modeled as suggested by Godeke *et al* in [19], where it is derived based on a microscopic description. The resulting expression published in the cited work is reproduced within the USL by choosing $\mu = 1$, $\nu = 1.52$, and $\eta = 2$ in equation (3).

For magnetometry simulations the self-field generated by the current loops within the sub-element is computed by applying the Biot–Savart law. The local magnetic field used for computing J_c of a current carrying element is calculated by taking the absolute value of the vector sum of the applied field and the self-field. In a multifilamentary wire, a sub-element is of course also subjected to self-field contributions generated by other sub-elements. These are, however, about one order of magnitude smaller, and are therefore neglected in

the simulations. For transport simulations the self-field is calculated in the same way as in our measurements on real samples (see section 2.2). One iteration step before outputting the final $J_c(T, B)$ results is usually sufficient. For simulating $B_{c2}(T)$ measurements, we run transport simulations in which the applied field is lowered in small steps from above B_{c2} until the condition $J_c > 10^6 \text{ A m}^{-2}$ is satisfied.

2.5. Pinning force scaling analysis

The program code used to carry out scaling analyses on both real and simulated results takes $J_c(B)$ data at various temperatures as input, and assumes that the critical currents are perpendicular to the magnetic field, leading to $F_p = |\vec{B} \times \vec{J}_c| = J_c B$. It then performs the following tasks to obtain the field scaling exponents p and q as well as the temperature dependence of the scaling field $B_{c2}^*(T)$.

- Localize the peak in $F_p(B)$ at each temperature. If the peak is not contained in the data, an extrapolation is used.
- Normalize all $F_p(B)$ curves to their respective peak value F_p^{\max} .
- Remove data points with volume pinning forces below a cut-off criterion. Such a procedure is commonly employed in scaling analyses, because ‘the tail does not scale’, as Ekin put it [2].
- Select reasonable initial values for the scaling exponents p and q .
- Fit $C_f b^p (1 - b)^q$ with $b = B/B_{c2}^*$ to the normalized data at each temperature, using the scaling field B_{c2}^* as fit parameter (the prefactor C_f normalizes the function to a peak value of 1).
- Assess the quality of the fit by calculating the global deviation (sum of the differences between the fit function and each normalized data point at all temperatures).
- Iterate p and q until the minimum in the global deviation is found with satisfactory accuracy.

This method finds the field scaling exponents which are the best compromise considering the entire temperature range. While the cut-off criterion can have a significant impact on the results, its choice is rather arbitrary. In this work we used a value of $0.2 \cdot F_p^{\max}$, i.e. the lowest 20% of the $F_p(B)$ values at each temperature were removed. Using an absolute value instead can lead to the complete exclusion of $F_p(B)$ curves obtained at high temperature, which is not in our interest here, since we want to discuss the influence of the analyzed temperature range.

The temperature scaling behavior is analyzed by fitting the function $F_p^{\max}(t) = F_p^{(0)} h(t)$ with $h(t)$ given by equation (3), and $t = T/T_c^*$ to the $F_p^{\max}(T)$ data obtained from the procedure described above. We fixed the exponents in $h(t)$ to the values $\nu = 1.52$, and $\mu = 1$, respectively. The former is a common choice motivated by a good agreement of the term $1 - t^\nu$ with the Maki-de Gennes expression for the temperature dependence of the upper critical field [19]. For μ the values 0, 1, and 2 are commonly used, the best choice being a matter of debate [2]. Both fixed exponents are consistent with the values used in the simulations (see

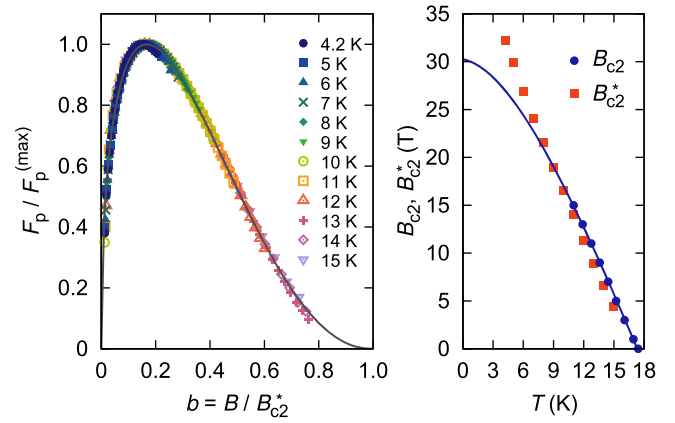


Figure 2. Scaling analysis results obtained from the examined RRP wire (conditions *mag/real*). Reasonably good scaling behavior (left plot) can be achieved, but only at the price of spurious scaling field values at low temperatures (right plot).

Table 1. Scaling analysis conditions used to examine the effects of experimental limitations.

Name	Type	T range	B_{\max}	I_{\max}
<i>mag/real</i>	magnetometry	4.2–15 K	7 T	—
<i>trans/real</i>	transport	4.2 K only	15 T	1 kA
<i>mag/full</i>	magnetometry	4.2–15 K	35 T	—
<i>trans/full</i>	transport	4.2–15 K	35 T	—

section 2.4). Our free parameters in the temperature scaling analysis are T_c^* and η . Note that although the simulations use the fixed value $\eta = 2$, as described in section 2.4, the scaling analysis can give a different result due to the effects of inhomogeneities, as discussed in section 3.2.

In the analyses of simulation results, we used additional conditions concerning the field range, the temperature range, and the maximum value of the current, to emulate the conditions of real measurements by removing data points which do not satisfy these conditions. This allows us to examine the effects of the experimental limitations on the results of the scaling analysis. The conditions referred to in the following are listed in table 1. The two with ‘*real*’ in their names are based on the limitations of our own experimental equipment (see sections 2.1 and 2.2), and the other two are for comparison with the ideal case, i.e. measurements without any limitations.

3. Results

3.1. Deviations from the expected behavior

We carried out pinning force scaling analyses as described in section 2.5 on magnetometry data (temperature range 4.2–15 K, 7 T maximum applied field) obtained from the RRP Nb₃Sn wire mentioned at the beginning of section 2. The left plot in figure 2 shows the thus obtained normalized pinning force function $f(b)$ (gray curve), and the scaled data points. The right plot compares the temperature dependence of the

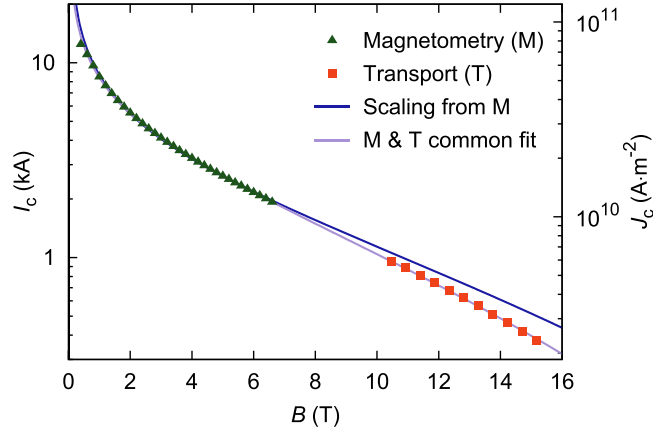


Figure 3. The scaling-based extrapolation of the magnetometry results (conditions *mag/real*) does not agree well with the transport critical current data. However, a common fit to magnetometry and transport data is possible without large deviations from either one of the data sets.

scaling field B_{c2}^* to that of the upper critical field determined from transport measurements.

The peak of the pinning force function in figure 2, which is located at $b_{\text{peak}} = p/(p + q)$, is not at the position 0.2, as it would be expected for grain boundary pinning (see [5]), but at $b = 0.17$. The obtained high-field exponent $q = 2.22$ does not deviate from the expected value $q = 2$ as strongly as in other wire types we investigated, but the discrepancy is significant enough to investigate its origin. A more problematic deviation from the expected behavior is exhibited by the scaling field, which takes on values much larger than the upper critical field at low temperatures. This obviously unphysical result is bound to lead to incorrect predictions of the volume pinning force at low temperatures and high magnetic fields. The problem is visualized in figure 3, where transport critical current data are compared to the $J_c(B)$ curve predicted based on the scaling analysis of magnetometry data. The latter strongly over-estimates the critical current density at high magnetic fields. A common fit to the transport data and the magnetometry data recorded at 4.2 K shows little deviation from either one of the data sets, and yields the parameters $p = 0.53$, $q = 2.69$, and $B_{c2}^* = 30.0$ T.

3.2. Effects of composition gradients on the scaling behavior

Owing to the solid state diffusion reaction in which the Nb_3Sn is formed within a wire, the resulting A-15 phase is never completely homogeneous. The remaining Sn concentration gradients within the A-15 phase were investigated by several researchers over the years [20–23]. Recent work on this subject matter as well as on other microstructural features was carried out by Tarantini *et al* [24, 25]

The Sn distribution within the sub-elements of the Ti-alloyed RRP wire discussed in this work was examined by means of EDX, as described in section 2.3. The thus obtained data, averaged over 15 sub-elements, are shown in figure 4. The distribution is normalized such that position 0 corresponds to the inner boundary of the A-15 phase (closest to the

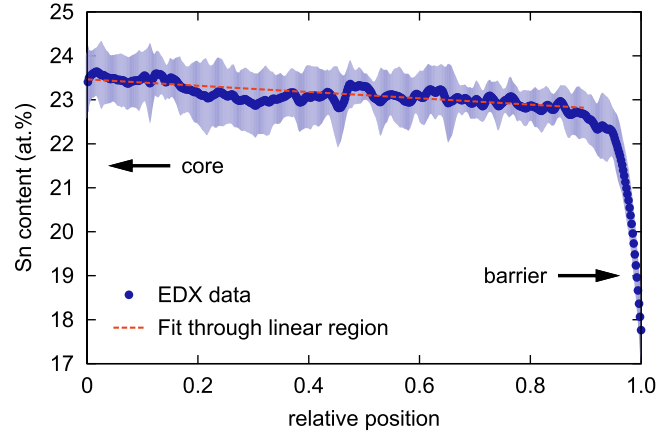


Figure 4. Sn distribution across the A-15 region of the sub-elements of the examined wire, obtained from EDX. The standard deviation $\pm\sigma$ of each data point is indicated by the light blue area.

Sn source), and position 1 corresponds to the outer boundary (where the Nb barrier is located). We found a relatively linear decrease of the Sn concentration over a wide range, followed by a steep fall-off near the barrier. A linear fit yields a difference in Sn concentration of 0.65 at% between the inner-most part of the sub-element and the outer end of the linear region, corresponding to $0.07 \text{ at}\% \mu\text{m}^{-1}$.

The effects of such Sn concentration gradients on the pinning force scaling behavior was examined using the simulation code described in section 2.4, and the scaling analysis algorithm outlined in section 2.5. Different simulation profiles were generated by varying the maximum Sn content β_{max} in the sub-elements, as well as the concentration gradient in the linear region. Since the sub-element dimensions were kept constant, we will specify the difference $\Delta\beta$ between β_{max} and the outer end of the linear region instead of the spatial derivative $d\beta/dr$. A fall-off similar to that in figure 4, starting at a relative position of 0.85 and modeled by a power function, was used in all profiles. The grain size was kept constant across the A-15 phase, and had the same value of 100 nm in all profiles (effects of grain size gradients were investigated separately, but found to be negligible in comparison to the effects of Sn concentration gradients). Consequently, we can refer to a simulation profile simply by specifying β_{max} and $\Delta\beta$. In the following, ‘the 24.5/0.5 wire’, for instance, will mean a wire with $\beta_{\text{max}} = 24.5 \text{ at}\%$, and $\Delta\beta = 0.5 \text{ at}\%$.

Figure 5 shows scaling analysis results obtained from three simulated wires. Their scaling exponents p and q , their zero-temperature scaling field values $B_{c2}^*(0)$ (WHH-extrapolated using equation (6)), their effective critical temperatures T_c^* , and their temperature scaling exponents η are listed in table 2. The conditions *mag/real* were used, i.e. the temperature and field range of the simulation output were cropped to match the experimental conditions (see section 2.1).

The scaling exponents obtained from the 24.5/0.5 wire are close to the theoretical grain boundary pinning values of $p = 0.5$ and $q = 2$, and its scaling field is in very good agreement with the upper critical field. Apparently, a high

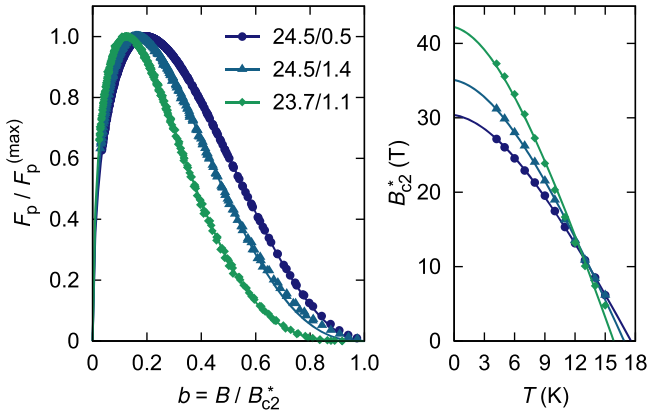


Figure 5. Scaling behavior of three simulated wires with different Sn distributions (conditions *mag/real*).

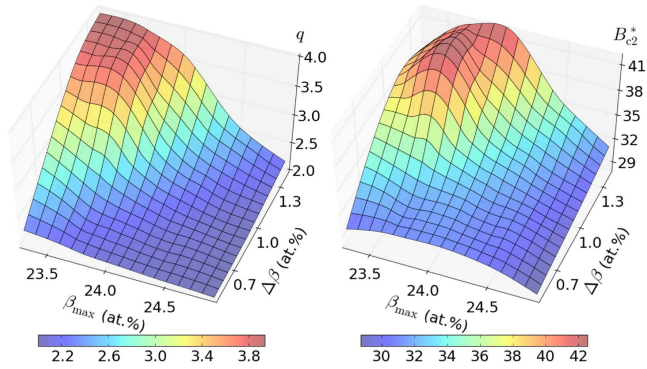


Figure 6. Variation of q and B_{c2}^* as function of β_{\max} and $\Delta\beta$, simulated using the conditions *mag/real*.

Table 2. Scaling parameters of the real wire and three simulated wires obtained under the conditions *mag/real*.

Wire	p	q	$B_{c2}^*(0)$ (T)	T_c^* (K)	η
real wire	0.45	2.22	34.5	17.3	2.32
24.5/0.5	0.49	2.03	30.3	17.7	2.17
24.5/1.4	0.50	2.58	35.0	16.9	2.25
23.7/1.1	0.51	3.65	42.1	15.6	2.26

value of β_{\max} and a small Sn concentration gradient do not lead to significant deviations. A larger gradient, realized in the 24.5/1.4 wire, however, produces a high-field exponent q of 2.58, and B_{c2}^* values which are somewhat larger than the upper critical field at low temperatures. This result qualitatively reproduces the behavior of the real wire, whose scaling characteristics are also specified in table 2 for comparison. The results obtained from the 23.7/1.1 wire show that the deviations become more extreme when β_{\max} is relatively low, even if a medium $\Delta\beta$ value is used.

The low-field parameter p remains almost unaffected, which stands to reason, given that the J_c suppression caused by inhomogeneities is much more pronounced at high-field values. The temperature scaling exponent η exhibits a moderate dependence on the Sn distribution, and takes on values slightly above 2, in agreement with real wires.

The pronounced effect of the Sn distribution within the sub-elements on q and B_{c2}^* is visualized in figure 6, which is based on simulation results obtained from 35 different profiles. There is a strong correlation between high values of q and high values of B_{c2}^* , and both are correlated with large Sn concentration gradients and low values of β_{\max} . This can be understood as follows: the value of q depends on the curvature of $F_p(B)$ in the high-field region, which is increased by inhomogeneities. At lower β_{\max} values the effect is more pronounced due to the nonlinearity of $T_c(\beta)$ and $B_{c2}(\beta)$. The scaling analysis algorithm attempts to find the one value for q which is the best match for the entire temperature range. However, it only knows the high-field $F_p(B)$ dependence at high temperatures, and in these data the peak in $f(b)$ is shifted to the left ($b_{\text{peak}} = p/(p+q) < 0.2$) by the high q value. Consequently, it shifts the low-temperature data to the left by increasing B_{c2}^* at low temperatures, in order to achieve scaling.

3.3. Results obtained from a realistic simulation profile

By running simulations with many different input profiles, we were able to find a profile which produces a good match with the magnetometry data obtained from the real wire in terms of the scaling parameters. We accomplished that by comparing the high-field exponent q , the magnitude of the volume pinning force F_p , the effective critical temperature T_c^* , and the zero-temperature scaling field $B_{c2}^*(0)$, and selecting the profile with the best overall agreement. We used a spatially constant grain size of 100 nm in all profiles, in agreement with the results obtained from examinations on a TEM lamella of the real wire. The values of the inner and outer sub-element radii were also chosen in accordance with the sub-element geometry found in the real wire.

The best matching profile was obtained using the values $\beta_{\max} = 24.4$ at%, and $\Delta\beta = 1.0$ at%, corresponding to a gradient of 0.10 at% μm^{-1} in the linear region. The fall-off starting at position 0.85 was modeled in general agreement with the EDX results shown in figure 4. The Sn distribution of this 24.4/1.0 wire profile as well as the resulting T_c and B_{c2} distributions are shown in figure 7. The Sn concentration gradient leads to a change in T_c of 1.7 K over the linear region, and to a B_{c2} distribution which has its maximum in the sub-element center due to the non-monotonicity of $B_{c2}(\beta)$ in the Li–Gao model.

The scaling parameters obtained from this 24.4/1.0 wire under the conditions *mag/real* are $p = 0.49$, $q = 2.22$, $B_{c2}^*(0) = 32.0$ T, $T_c^* = 17.1$ K, and $\eta = 2.20$. The high-field exponent q of the real wire can be reproduced accurately, and the temperature scaling parameters are in good agreement. The zero-temperature scaling field is somewhat low, the Sn concentration gradient of the profile is 40% higher than in the real wire, and the β_{\max} value is higher by 1 at%. These deviations are probably owed to the limited accuracy of the model describing the intrinsic properties, in particular to the fact that it does not take into account the effects of additives on $T_c(\beta)$ and $B_{c2}(\beta)$.

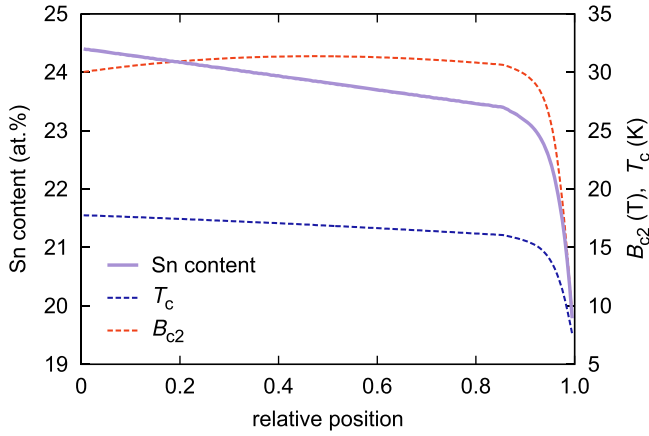


Figure 7. Sn concentration and intrinsic properties calculated from it as a function of position (0 = core/A-15 boundary, 1 = A-15/barrier boundary) of the simulation profile which produces the best match to the real wire.

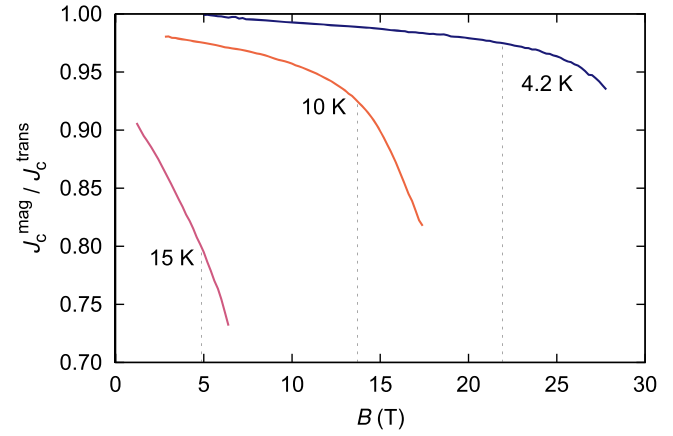


Figure 9. Illustration of the greater sensibility to inhomogeneities of magnetometry-based J_c data relative to transport results (self-field corrected). The markers indicate $0.8 B_{c2}$ at the respective temperature.

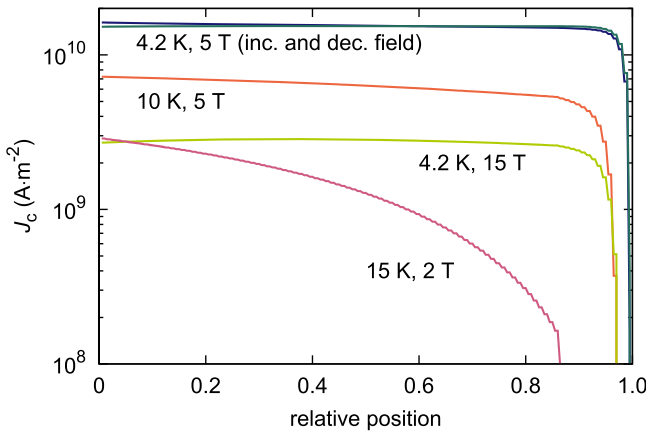


Figure 8. J_c distributions across the A-15 layer of the best matching simulated wire at different temperatures and applied fields.

Figure 8 illustrates the effect of the inhomogeneity of the 24.4/1.0 wire on the J_c distribution within a sub-element in a magnetometry simulation. The relative position refers to a radial line across the A-15 region perpendicular to the applied field, position 0 corresponding to the inner, and position 1 to the outer boundary. Two curves are shown for $T = 4.2$ K and $B = 5$ T, showing the differences between increasing (blue) and decreasing applied field (green) due to the self-field contribution. For the other shown T - B combinations, the difference would not be clearly visible in the logarithmic plot due to the much lower J_c . While the critical current density is relatively constant across the A-15 area at 4.2 K and 5 T, a significant variation can be seen at the same field when the temperature is increased to 10 K. Going back to $T = 4.2$ K, and increasing the field to 15 T leads to a distribution with the maximum value in the center of the A-15 region, which is caused by the B_{c2} profile shown in figure 7. Note that for positions larger than ~ 0.8 , the decrease of J_c is comparable to the one found at 10 K and 5 T, although the temperature is much lower, and the field is still far below B_{c2} . At 15 K the decline of J_c across the A-15 region is extreme, even at low fields.

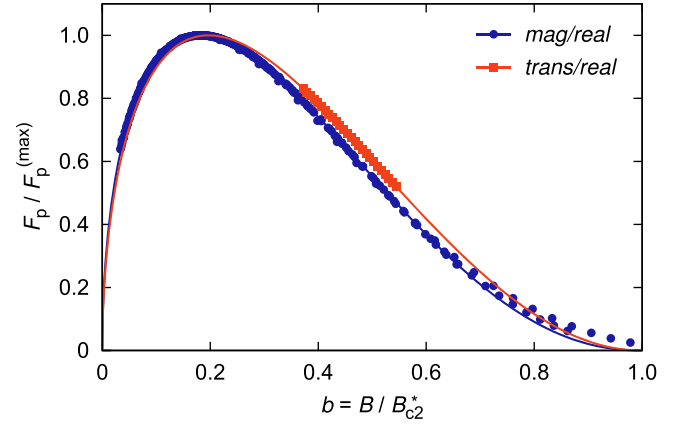


Figure 10. Pinning force functions obtained under the conditions *mag/real* and *trans/real* (24.4/1.0 wire). The data points on which the analysis is based are also shown.

3.4. Magnetometry versus transport

J_c data obtained from magnetometry are more strongly affected by inhomogeneities than transport measurements, since current loops encompassing a larger area contribute more to the total magnetic moment of the sample. As a result, magnetometry tends to underestimate the average critical current density, because contributions from currents flowing near the barrier of a sub-element, where J_c is low, receive a higher weighting. This effect is visualized in figure 9, where the ratio of the J_c values obtained from magnetometry and from transport simulations (self-field corrected) of the 24.4/1.0 wire is plotted for different temperatures. The vertical markers are located at the field $B = 0.8 B_{c2}$ of the respective temperature to facilitate a comparison. While the discrepancy is negligible at 4.2 K and tolerable at 10 K, as long as a reasonable cut-off criterion is used in the scaling analysis, the deviation at 15 K is problematic. Even at low applied field values a reduction of $\sim 10\%$ is found, and at $0.8 B_{c2}$ it increases to 20%.

Figure 10 shows a comparison of the pinning force functions obtained from scaling analyses of the 24.4/1.0 wire

under realistic experimental conditions for magnetometry (*mag/real*) and transport (*trans/real*), respectively. There is a distinct discrepancy between the two curves, which is influenced by three factors. Firstly, the peak in the transport data is not within the covered field range, thus calling for an extrapolation, which can be a source of error. Secondly, the magnetization data in the reduced field range where transport data are available were obtained at significantly higher temperatures, which means they are more strongly affected by inhomogeneities. And thirdly, the high temperature magnetometry data near $b = 1$ cause an increase of q and B_{c2}^* through the suppression of J_c due to inhomogeneities. Note that it is not clear which one of the two pinning force functions is 'better'. After all, any scaling-based description of the volume pinning force of an inhomogeneous sample is inherently flawed to some degree.

3.5. Influence of the analyzed temperature range

Analyzing pinning force data of the simulated 24.4/1.0 wire, which cover the entire reduced field range even at low temperatures, produces a relatively good overall agreement between the thus obtained pinning force function and the input data. In this case medium deviations occur over a wide b range, instead of small deviations in a limited range, and large discrepancies outside of this range, as it can happen when analyzing data which cover a limited field range only. The differences in the scaling parameters between magnetometry and transport when the full field range up to B_{c2} is analyzed (i.e. conditions *mag/full* and *trans/full*) are small, since the evaluation-immanent reduction of the magnetometry-based J_c at high temperature and field values relative to transport results (see figure 9) is mitigated by the presence of low-temperature high-field data.

In a real experiment where the available maximum field is limited to $B \ll B_{c2}$, an obvious strategy for reducing a detrimental influence of inhomogeneities is to lower the upper limit of the temperature range used in the scaling analysis. This is, of course, a compromise in terms of the covered reduced field range. The scaling parameters q and $B_{c2}^*(0)$ as a function of the upper temperature limit (the lower limit was always 4.2 K), obtained from the 24.4/1.0 wire using magnetometry with a maximum field of 7 T, are shown in figure 11. Analyzing the full field range instead, i.e. using the conditions *mag/full* yields the parameters $q = 2.09$ and $B_{c2}^*(0) = 31.0$ T, which are indicated by gray bars in the plot. Their intersection with the 7 T field range curves indicates that 13 K would be a reasonable value for the upper temperature limit, corresponding to $0.73 T_c^{\max}$, where T_c^{\max} is the highest T_c value (transition onset) occurring in the wire. At this temperature a maximum field of 7 T covers approximately two thirds of the reduced field range.

4. Discussion

It is easy to understand that the volume pinning force of an inhomogeneous superconductor cannot be correctly described

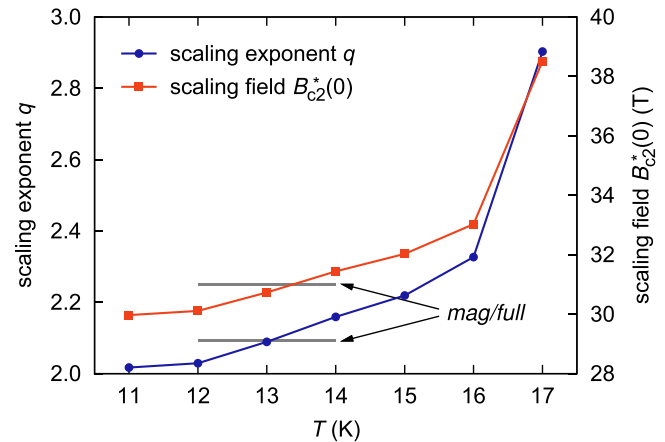


Figure 11. Change of the scaling parameters as a function of the upper temperature limit for magnetometry with 7 T maximum applied field. The values obtained under the conditions *mag/full* are indicated by gray bars.

by a scaling expression, since it does not exhibit a single T_c and B_{c2} value, but a distribution instead. This does of course not imply that scaling is useless when inhomogeneities are present. Provided that the characterization was done properly, the obtained scaling parameters can very well give an accurate $J_c(T, B)$ prediction within the technologically relevant temperature and field range. Nevertheless, inhomogeneities—even in the form of relatively small composition gradients—lead to deviations from the ideal scaling behavior, and the pitfalls arising from this effect are certainly often underestimated, especially when the characterization is based on magnetometry.

The problem that the B_{c2}^* obtained from magnetometry takes on unreasonably high values at low temperatures was previously reported by Ekin in [3] (figure 15(b)), where transport- and magnetometry-based scaling analysis results obtained from a Ta-alloyed RRP wire are compared. We showed that the pronounced decline of J_c across the A-15 region at high temperatures (see section 3.3), to which magnetometry-based J_c data are more sensitive (see section 3.4), causes this effect, and also strongly affects the high-field exponent q .

While the effect of Sn concentration gradients on the J_c distribution and consequently on the scaling behavior are very distinct, our simulations showed a comparatively small impact of grain size gradients on the scaling parameters. However, there is literature which suggests that scaling is affected by pronounced grain morphology features such as the two grain populations (small equiaxed and larger columnar grains) present in bronze route wires [26]. The large Sn concentration gradients in the filaments of such wires are of course also expected to have a strong impact on the scaling behavior. In a perhaps forgotten work (last cited in 1998 at the time of writing), Alterovitz and Woollam suggest to deal with inhomogeneities by using a redefined reduced field [27]. In that way scaling can be restored at low fields, which may be useful for determining the pinning mechanism based on the peak position in $f(b)$.

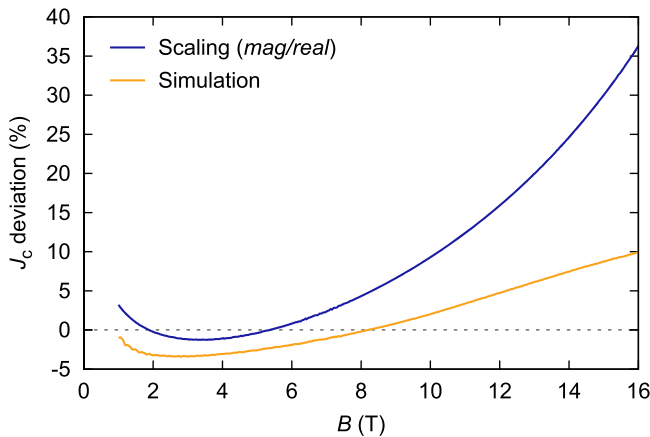


Figure 12. Comparison of the deviation of $J_c(B)$ based on scaling analysis results obtained from magnetometry data (real wire; blue curve), and $J_c(B)$ obtained from simulations of the best matching profile (24.4/1.0 wire; orange curve), relative to the common fit to magnetometry and transport data of the real wire obtained at 4.2 K.

A popular method related to pinning force scaling is the so-called Kramer extrapolation, which is used to obtain B_{c2} from $J_c(B)$ data [28]. It assumes that the scaling exponents are $p = 0.5$ and $q = 2$, which inevitably leads to problems at high temperature and field values where inhomogeneities induce an increase in q . Some caution is also in order when the WHH extrapolation method is used on $B_{c2}(T)$ data obtained from low current transport measurements similar to those described in section 2.2. Inhomogeneities cause deviations from the WHH temperature dependence (equation (6)), leading to an underestimation of B_{c2} at low temperatures, if the maximum applied field is not high enough.

In section 3.1 we showed that the scaling parameters obtained from magnetometry with a maximum field of 7 T can lead to very inaccurate predictions for the high-field J_c at low temperatures. As pointed out above, a well chosen upper limit for the temperature range can help reduce the deviations. However, in some cases more accurate results may be obtained by modeling the inhomogeneities, in particular the Sn distribution, based on $J_c(B, T)$ data (i.e. finding the best matching profile, as discussed in section 3.3), or, if available, based on EDX data. Figure 12 compares the deviations of $J_c(B)$ obtained from the scaling analysis of the real wire (7 T field range, 4.2–15 K temperature range), and from the simulation of the best matching profile, relative to the actual $J_c(B)$ obtained at 4.2 K from magnetometry and transport measurements ('M & T common fit' in figure 3). In this case the simulation is clearly superior to the scaling-based high-field $J_c(B)$ prediction, namely by a factor of three at 4.2 K and 15 T.

A better understanding of Sn concentration gradients from a materials science point of view is likely to improve both our ability to model the superconducting properties of Nb_3Sn wires and the manufacturing techniques employed in their production. A model describing the diffusion process occurring during the formation of Nb_3Sn was developed by Xu and Sumption [29, 30]. This model may help advance our understanding of the differences in terms of stoichiometry and

grain morphology between various wire designs and different heat treatments. For accurately modeling ternary Nb_3Sn wires based on EDX data, the influence of additives on $T_c(\beta)$ and $B_{c2}(\beta)$ must be known. Experimental data on these dependences were collected for instance by Suenaga *et al*, but to our knowledge a reliable model has not been devised yet [31]. Using such a model in our simulations (which currently model a Ti-alloyed wire using the best matching binary Nb_3Sn profile) would probably further improve its $J_c(B)$ prediction, which is why in our opinion research on this subject is called for.

5. Conclusions

In this article we presented a detailed analysis of the effects of A-15 phase inhomogeneities, in particular radial Sn concentration gradients within sub-elements, on the pinning force scaling behavior of Nb_3Sn wires, including a discussion on the influence of the experimental procedure. The main conclusions of our work can be summarized as follows.

Magnetometry is more sensitive to inhomogeneities than transport measurements, since the largest current loops flow near the sub-element barrier, where J_c is strongly suppressed. This leads to an underestimation of the average critical current density. When characterizing $J_c(T, B)$ of Nb_3Sn samples, and the maximum applied field is relatively low (e.g. 7 T SQUID magnetometer), one can buy a reasonably good scaling behavior in a limited field range at the price of a nonsensical temperature dependence of the scaling field. The consequence is that at high field values the behavior of the samples will deviate significantly from predictions made based on the scaling analysis. Despite the problems arising from inhomogeneities, scaling analyses can be technologically useful, if carried out with care, i.e. with the potential pitfalls in mind. A combination of transport measurements and magnetometry, where the latter is used to refine the scaling parameters T_c^* and η could turn out to be particularly useful, as speculated by Ekin [32]. For predicting the high-field J_c of Nb_3Sn wires based on low-field magnetometry data, we recommend selecting a sensible upper limit of the temperature range included in scaling analyses in order to mitigate the effects of inhomogeneities. A temperature of 13 K appears to be a good upper limit for typical wires, if the maximum applied field is around 7 T. If significantly higher fields are available, the upper limit can be reduced such that $b \approx 2/3$ is reached at the highest temperature.

Acknowledgments

We gratefully acknowledge CERN for funding the research at Atominstut and USTEM under the collaboration agreement KE3194, and in particular Christian Scheuerlein for taking care of the sample heat treatments. We also thank Jack Ekin for fruitful discussions which helped improve the comprehensibility of this article. The authors acknowledge the TU Wien University Library for financial support through its Open Access Funding Program.

ORCID iDs

T Baumgartner  <https://orcid.org/0000-0002-2228-1072>

J Bernardi  <https://orcid.org/0000-0002-4626-9246>

M Eisterer  <https://orcid.org/0000-0002-7160-7331>

References

- [1] Fietz W A and Webb W W 1969 *Phys. Rev.* **178** 657
- [2] Ekin J W 2010 *Supercond. Sci. Technol.* **23** 083001
- [3] Ekin J W 2016 *Supercond. Sci. Technol.* **29** 123002
- [4] Ekin J W 2017 *Supercond. Sci. Technol.* **30** 033005
- [5] Dew-Hughes D 1974 *Phil. Mag.* **30** 293
- [6] Cooley L D, Fischer C M, Lee P J and Larbalestier D C 2004 *J. Appl. Phys.* **96** 2122
- [7] Baumgartner T, Eisterer M, Weber H W, Flükiger R, Bordini B, Bottura L and Scheuerlein C 2012 *IEEE Trans. Appl. Supercond.* **22** 6000604
- [8] Bordini B 2010 Self-field correction in critical current measurements of superconducting wires tested on ITER VAMAS barrels *CERN-ITER Collaboration Report Internal Note* 2010-38
- [9] Helfand E and Werthamer N R 1964 *Phys. Rev. Lett.* **13** 686
- [10] Helfand E and Werthamer N R 1966 *Phys. Rev.* **147** 288
- [11] Werthamer N R, Helfand E and Hohenberg P C 1966 *Phys. Rev.* **147** 295
- [12] Baumgartner T, Eisterer M, Weber H W, Flükiger R, Scheuerlein C and Bottura L 2014 *Supercond. Sci. Technol.* **27** 015005
- [13] Li Y and Gao Y 2017 *Sci. Rep.* **7** 1133
- [14] Suenaga M 1985 *IEEE Trans. Magn.* **21** 1122
- [15] Flükiger R, Uglietti D, Senatore C and Buta F 2008 *Cryogenics* **48** 293
- [16] Mentink M G T, Dhalle M J J, Dietderich D R, Godeke A, Hellman F and ten Kate H H J 2017 *Supercond. Sci. Technol.* **30** 025006
- [17] Godeke A 2006 *Supercond. Sci. Technol.* **19** R68
- [18] Fischer C M 2002 Investigation of the relationships between superconducting properties and Nb₃Sn reaction conditions in powder-in-tube Nb₃Sn conductors *Master's Thesis* University of Wisconsin-Madison
- [19] Godeke A, ten Haken B, ten Kate H H J and Larbalestier D C 2006 *Supercond. Sci. Technol.* **19** R100
- [20] Hawes C D, Lee P J and Larbalestier D C 2000 *IEEE Trans. Appl. Supercond.* **10** 988
- [21] Hawes C D, Lee P J and Larbalestier D C 2006 *Supercond. Sci. Technol.* **19** S27
- [22] Godeke A, den Ouden A, Nijhuis A and ten Kate H H J 2008 *Cryogenics* **48** 308
- [23] Cantoni M, Scheuerlein C, Pfirter P-Y, de Borman F, Rossen J, Arnau G, Oberli L and Lee P 2010 *J. Appl. Phys.: Conf. Ser.* **234** 022005
- [24] Tarantini C, Lee P J, Craig N, Ghosh A and Larbalestier D C 2014 *Supercond. Sci. Technol.* **27** 065013
- [25] Tarantini C, Segal C, Sung Z H, Lee P J, Oberli L, Ballarino A, Bottura L and Larbalestier D C 2015 *Supercond. Sci. Technol.* **28** 095001
- [26] Flükiger R, Senatore C, Cesaretti M, Buta F, Uglietti D and Seeber B 2008 *Supercond. Sci. Technol.* **21** 054015
- [27] Alterovitz S A and Woollam J A 1978 *Phil. Mag. B* **38** 619
- [28] Kramer E J 1973 *J. Appl. Phys.* **44** 1360
- [29] Xu X and Sumption M D 2016 *Sci. Rep.* **6** 19096
- [30] Xu X 2017 *Supercond. Sci. Technol.* **30** 093001
- [31] Suenaga M, Welch D O, Sabatini R L, Kammerer O F and Okuda S 1986 *J. Appl. Phys.* **59** 840
- [32] Ekin J W 2018 private communication